The Astrophysical Journal, 791:41 (16pp), 2014 August 10 doi:10.1088/0004-637X/791/1/41

THE ORIGIN OF THE X-RAY EMISSION FROM THE HIGH-VELOCITY CLOUD MS30.7−81.4−118

David B. Henley[1], Robin L. Shelton[1], and Kyujin Kwak[2]
[1] Department of Physics and Astronomy, University of Georgia, Athens, GA 30602, USA; dbh@physast.uga.edu, rls@physast.uga.edu
[2] School of Natural Science, Ulsan National Institute of Science and Technology (UNIST), 50 UNIST-gil, Ulju-gun, Ulsan 689-798, Korea; kkwak@unist.ac.kr
Received 2014 February 13; accepted 2014 June 23; published 2014 July 24

ABSTRACT

A soft X-ray enhancement has recently been reported toward the high-velocity cloud MS30.7−81.4−118 (MS30.7), a constituent of the Magellanic Stream. In order to investigate the origin of this enhancement, we have analyzed two overlapping *XMM-Newton* observations of this cloud. We find that the X-ray enhancement is ∼6′ or ∼100 pc across, and is concentrated to the north and west of the densest part of the cloud. We modeled the X-ray enhancement with a variety of spectral models. A single-temperature equilibrium plasma model yields a temperature of $(3.69^{+0.47}_{-0.44}) \times 10^6$ K and a 0.4–2.0 keV luminosity of 7.9×10^{33} erg s^{-1}. However, this model underpredicts the on-enhancement emission around 1 keV, which may indicate the additional presence of hotter plasma ($T \gtrsim 10^7$ K), or that recombination emission is important. We examined several different physical models for the origin of the X-ray enhancement. We find that turbulent mixing of cold cloud material with hot ambient material, compression or shock heating of a hot ambient medium, and charge exchange reactions between cloud atoms and ions in a hot ambient medium all lead to emission that is too faint. In addition, shock heating in a cool or warm medium leads to emission that is too soft (for reasonable cloud speeds). We find that magnetic reconnection could plausibly power the observed X-ray emission, but resistive magnetohydrodynamical simulations are needed to test this hypothesis. If magnetic reconnection is responsible for the X-ray enhancement, the observed spectral properties could potentially constrain the magnetic field in the vicinity of the Magellanic Stream.

Key words: Galaxy: halo – ISM: clouds – ISM: individual objects (MS30.7−81.4−118) – X-rays: ISM

Online-only material: color figures

1. INTRODUCTION

High-velocity clouds (HVCs) are clouds in the Galactic halo with high line-of-sight velocities ($\gtrsim$90 km s^{-1}) relative to the local standard of rest (Wakker & van Woerden 1997). These clouds may be condensations from a Galactic fountain falling back toward the disk, gas stripped off satellite galaxies, or extragalactic gas left over from the formation of the Local Group galaxies (see Bregman 2004 for a review). Note that not all HVCs need have the same origin, and more than one of the aforementioned processes may have been involved in the creation of the Galaxy's population of HVCs. HVCs were originally discovered from observations of 21 cm H I emission (Muller et al. 1963), and a recent survey of moderate and high Galactic latitudes found high-velocity H I on 37% of sight lines (Lockman et al. 2002). However, high-velocity material is also observed via other lines, including those of high ions such as C IV, N V, and O VI (Sembach et al. 2003; Fox et al. 2004, 2005, 2006; Collins et al. 2007). The high-velocity material bearing these high ions ($T \sim (1–3) \times 10^5$ K) is likely produced from the interactions of HVCs with a hot ($T \gtrsim 10^6$ K) ambient medium (Sembach et al. 2003; Fox et al. 2004; Collins et al. 2007; Kwak et al. 2011).

The interactions of HVCs with their surroundings may also produce soft X-ray emission. Several authors have reported excess soft X-ray emission (above the level of the diffuse X-ray background) associated with some HVCs. The early reports were based on Wisconsin, *SAS-3*, and *HEAO-1* survey data of the Complex C region (Hirth et al. 1985), a pointed *ROSAT* observation of HVC 90.5+42.5−130 (Kerp et al. 1994), and *ROSAT* All-Sky Survey data of several different HVC complexes (Herbstmeier et al. 1995; Kerp et al. 1996, 1999). For the HVC complexes, their reported X-ray excesses are ∼1°–10° in size (Herbstmeier et al. 1995; Kerp et al. 1996, 1999). However, the conclusion that these X-ray excesses are physically associated with the HVCs has been disputed, on the grounds that these studies did not adequately take into account the possibility of small-scale variations in the brightnesses of the Galactic halo and/or the Local Bubble (Wakker & van Woerden 1997; Wakker et al. 1999). Better data at lower energies (where the absorption is higher) are needed to constrain the location of these X-ray excesses relative to the Galaxy's H I (Wakker et al. 1999).

More recently, higher spatial resolution observations with *XMM-Newton* and *Chandra* show evidence for excess X-ray emission (on the scale of a few arcminutes) associated with other, more compact HVCs (Bregman et al. 2009).[3] The small spatial scales compared with the above-mentioned studies increase the confidence that the associations between these X-ray excesses and the corresponding HVCs are real. The best evidence comes from an *XMM-Newton* observation of the HVC MS30.7−81.4−118 (hereafter MS30.7), which is a constituent of the Magellanic Stream (Mathewson et al. 1974; Putman et al. 2003). Bregman et al. (2009) were looking for shadowing (i.e., partial blocking) of the X-ray emission expected from the warm–hot intergalactic medium (Cen & Ostriker 1999), and thus hoped to see a reduction in the X-ray count rate toward the densest part of the cloud. Instead, they found that 0.4–1.0 keV count rate measured with the pn detector toward the densest part of the cloud was 0.64 ± 0.10 counts ks^{-1} arcmin^{-2} higher than the off-cloud background rate (2.54 versus 1.90 counts ks^{-1} arcmin^{-2}). Bregman et al. (2009) also found on-cloud X-ray excesses (albeit less significant) in *Chandra* observations

[3] Note that the *XMM-Newton* and *Chandra* data are also of higher spectral resolution than the earlier data. However, Bregman et al. (2009) did not report on the spectra of the X-ray excesses that they observed.

Table 1
MS30.7 Observation Details

Obs.	Start	R.A.	Decl.	t_{exp}	t_{clean} (ks)		
ID	date	(J2000)	(J2000)	(ks)	MOS1	MOS2	pn
(1)	(2)	(3)	(4)	(5)	(6)	(7)	(8)
0204670101	2004 Jan 03	00 12 56.3	−27 12 06.7	51.9	44.1	43.7	35.6
0670780101	2011 Jul 01	00 14 08.7	−27 11 01.2	61.5	33.1	35.9	22.0

Notes. Column 5 contains the observation exposure time, while Columns 6–8 contain the usable exposure times for each camera after cleaning.

of MS30.7 and of another HVC, CHVC 125+41−207. They attributed the greater significance of the enhancement in the *XMM-Newton* observation of MS30.7 to *XMM-Newton*'s larger field of view, which allowed for greater contrast between the on- and off-cloud regions.

If the observed X-ray excesses are physically associated with HVCs, then they undoubtedly arise from the interaction of the clouds with their environment. However, the detailed mechanism is uncertain. Various mechanisms have been proposed: shock heating (Hirth et al. 1985; Bregman et al. 2009; Shelton et al. 2012), compression of an already hot ambient medium (Herbstmeier et al. 1995), magnetic reconnection (Kerp et al. 1994, 1996; Zimmer et al. 1997), charge exchange (CX) reactions between neutral atoms in the cloud and ions in a hot ambient medium (Lallement 2004), and turbulent mixing of the cold cloud material with a hot ambient medium (Shelton et al. 2012). Regardless of the specific mechanism, the resulting X-ray spectrum and brightness will depend, at least in part, on the ambient conditions in the vicinity of the HVC. As a result, understanding the mechanism behind the X-ray emission from HVCs could potentially provide constraints on quantities such as the density, the pressure, or the magnetic field in the Galactic halo. Note that at the distance of the Magellanic Stream (∼60 kpc), few such constraints exist.

In this paper, we analyze two *XMM-Newton* observations of MS30.7, with the goal of understanding the mechanism responsible for the X-ray enhancement reported by Bregman et al. (2009). The first observation is that analyzed by Bregman et al., while the second is to the east of the first (Section 2). We use these observations to create an X-ray image of MS30.7 and its surroundings, so we can more clearly see the extent and morphology of the X-ray enhancement (Section 2.2). We extract (Section 2.3) and analyze (Section 3) the spectrum of the X-ray enhancement, using a variety of spectral models. We then use these results to test different physical models for the origin of the X-ray emission (Section 4). In particular, we examine turbulent mixing with or compression of a hot ambient medium (Section 4.2), shock heating (Section 4.3), CX (Section 4.4), and magnetic reconnection (Section 4.5). We discuss our results in Section 5, and finish with our summary and conclusions in Section 6.

2. OBSERVATIONS AND DATA REDUCTION

The details of the two *XMM-Newton* observations of MS30.7 are shown in Table 1. The first observation (observation ID 0204670101) was previously analyzed by Bregman et al. (2009). The second observation (observation ID 0670780101), carried out 7.5 yr later, has its pointing direction ≈14′ to the east of that of the first observation. Since the radius of the *XMM-Newton* field of view is ≈14′, the fields overlap.

2.1. Initial Data Reduction

We reduced the data using the *XMM-Newton* Extended Source Analysis Software[4] (*XMM*-ESAS; Snowden & Kuntz 2012), as distributed with version 12.0.1 of the *XMM-Newton* Science Analysis Software[5] (SAS). We first used the standard SAS `emchain` and `epchain` scripts to produce calibrated events list for each exposure (i.e., for each camera from each observation). We then used the *XMM*-ESAS `mos-filter` and `pn-filter` scripts to excise periods of soft-proton flaring from the data (essentially, these scripts remove from the data periods of time whose count rates differ by more than 1.5σ from the typical count rate). The usable time that remained after this cleaning is shown for each camera in the final three columns of Table 1.

Note that the soft-proton filtering yields systematically less time for the pn camera than for the MOS cameras. This is most likely due to the fact that the pn camera is more sensitive than the MOS cameras. As a result, in the absence of any flaring (i.e., if the count rate variations were due solely to Poissonian fluctuations), the count rate distribution would be narrower, relative to the mean count rate, for the pn camera than for the MOS cameras. This means that relatively smaller excursions from the mean count rate would be flagged as soft proton flares in the pn data than in the MOS data, resulting in more time being filtered out of the pn data.

We next used the SAS `edetect_chain` script to detect sources whose 0.5–2.0 keV flux exceeded 2×10^{-15} erg cm^{-2} s^{-1}. We analyzed each observation individually, using the data from the MOS1, MOS2, and pn cameras simultaneously. We excluded the detected sources from the data using circular exclusion regions. For a given source, the source exclusion radius was equal to the semimajor axis of the ellipse on which the source count rate per pixel is 0.2 times the local background count rate. This radius depends on the source brightness relative to the local background. The source exclusion regions for the two observations were merged before the sources were excised. Hence, if a source lying in the overlap region was detected in both observations, it was excised using the larger of the two source exclusion regions resulting from the analysis of the individual observations. Also, if a source in the overlap region was detected in only one observation, the region surrounding it was excised from both observations. This approach of merging the source exclusion regions is conservative in terms of minimizing contamination of the diffuse emission from point sources.

2.2. X-Ray Image Creation

We used *XMM*-ESAS tools to create a mosaicked 0.4–1.2 keV image of MS30.7. The upper limit of this energy band was

[4] http://heasarc.gsfc.nasa.gov/docs/xmm/xmmhp_xmmesas.html
[5] http://xmm.esac.esa.int/sas/

chosen to maximize the width of the band while avoiding contamination from the instrumental Al fluorescence line at 1.49 keV. We first used the `mos_back` and `pn_back` programs to generate images of the 0.4–1.2 keV quiescent particle background (QPB) for each exposure. These programs use databases of filter-wheel-closed data to construct the QPB image; these data were scaled to our observations using data from the unexposed corner pixels that lie outside the field of view (Kuntz & Snowden 2008). We then used the `merge_comp_xmm` program to combine the images of the 0.4–1.2 keV events from all three cameras and from both observations (i.e., a total of six images were combined to make the resulting merged image). Similarly, we used `merge_comp_xmm` to combine the QPB images and the exposure maps. Finally, we subtracted the combined QPB image from the combined events image, divided this background-subtracted image by the exposure map, and adaptively smoothed the resulting flat-fielded image, using the *XMM*-ESAS `adapt_2000` program. This program also filled in the chip gaps and the holes in the data resulting from the point source removal, using data from neighboring pixels.

The resulting X-ray image of MS30.7 is shown in Figure 1. The X-ray enhancement reported by Bregman et al. (2009) is near the center of the image. The enhanced X-ray emission is concentrated near the northern and western edges of the highest H I contour. There appears to be a gap between the northern and western portions of the enhanced emission, but this may be an artifact due to the removal of a point source at $(\alpha, \delta) = (00^{\rm h}13^{\rm m}16^{\rm s}, -27^{\circ}11'16'')$ (see upper panel of Figure 1). Overall, the enhancement is $\sim 6'$ across, corresponding to 100 pc at a distance of 60 kpc.

In addition to the X-ray enhancement reported by Bregman et al. (2009), there is another bright region of similar diameter at the bottom-center of the field, as well as a smaller bright region a few arcminutes to the southeast of the enhancement. Neither of these additional bright regions is correlated with the HVC H I, raising the possibility that the enhancement reported by Bregman et al. (2009) is not physically associated with MS30.7, but is just the result of a chance alignment. If we assume that two bright regions similar in size to the enhancement is typical for a field the size of that covered by Figure 1, we can estimate the probability that at least one of these bright regions will be aligned by chance with (say, within $3'$ of) the densest part of the HVC. The field covered by Figure 1 is 1079 arcmin^2, and so this probability is $1-(1-\pi \times 3^2/1079)^2 = 5\%$. This probability is not so small that we can confidently rule out a chance alignment. However, the fact that the enhancement emission tends to "wrap around" the 4×10^{20} cm^{-2} contour does support the conclusion that the enhancement emission is indeed physically associated with MS30.7. We will further consider this issue in Section 5.1.

2.3. Spectral Extraction

For each camera from each observation, we extracted a 0.4–5.0 keV spectrum of the X-ray enhancement, and a corresponding off-enhancement spectrum, used to constrain the sky background. The spectral extraction regions are shown in the lower panel of Figure 1. The central "n"-shaped region is the spectral extraction region for the enhancement—we used the same extraction region for both observations. The left and right regions are the regions used to extract the off-enhancement spectra from observations 0670780101 and 0204670101, respectively. The shapes of these regions were chosen by following the 2×10^{20} cm^{-2} H I contour and the edge of the pn field of view.

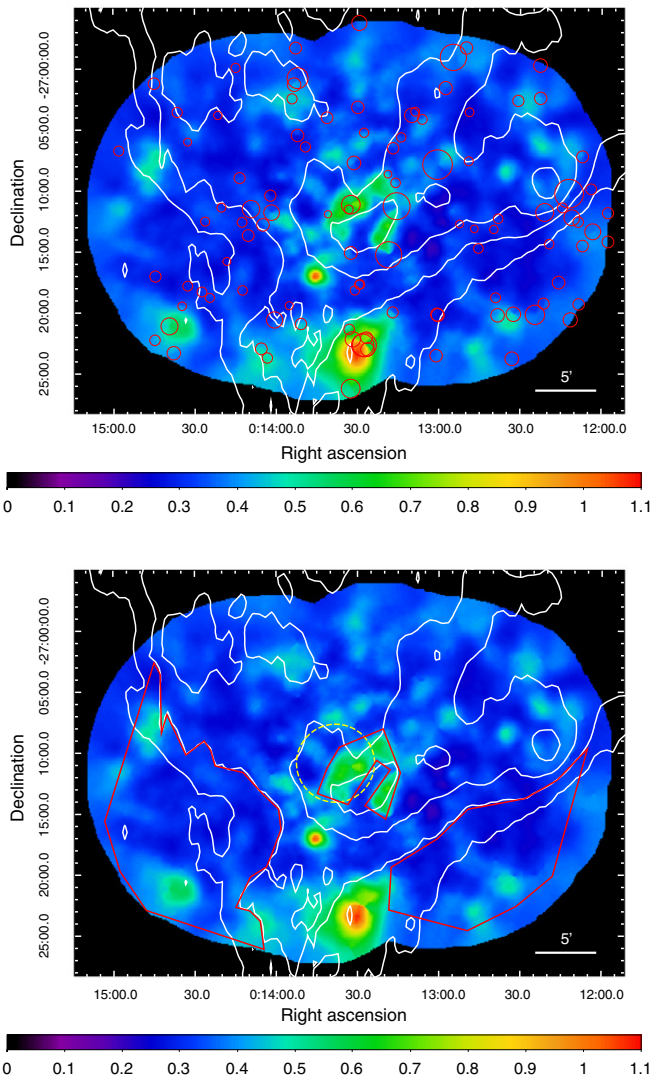

Figure 1. Mosaicked, QPB-subtracted, flat-fielded 0.4–1.2 keV images of MS30.7, created by combining data from the MOS1, MOS2, and pn cameras. The color scales are in MOS2 counts ks^{-1} arcmin^{-2}; the data from the other cameras were rescaled to match the response of the MOS2 camera. The contours indicate H I column densities of 1, 2, 3, and 4×10^{20} cm^{-2} for a velocity interval of -155 to -80 km s^{-1} relative to the local standard of rest (from a combination of Parkes (Brüns et al. 2005) and unpublished Australia Telescope Compact Array (ATCA) data (C. Brüns 2011, private communication)). In the upper panel, the image is overlaid with circles indicating the point source exclusion regions (Section 2.1); the holes in the data resulting from the source removal have been filled in using data from neighboring pixels. In the lower panel, the image is overlaid with the regions from which spectra were extracted (red polygons; Section 2.3). The dashed yellow circle indicates the position and estimated size of the galaxy group MZ 01537 (see Section 5.1).

(A color version of this figure is available in the online journal.)

We used the *XMM*-ESAS `mos-spectra` and `pn-spectra` scripts to extract the X-ray spectra from the data. We regrouped the X-ray spectra such that each bin contained at least 25 counts. The spectral extraction scripts also calculated the corresponding response files needed for the analysis—the redistribution matrix files and ancillary response files—using the SAS `rmfgen` and `arfgen` programs, respectively.

From each X-ray spectrum we subtracted the corresponding QPB spectrum, calculated using the *XMM*-ESAS `mos_back` or `pn_back` program. Similarly to the QPB images used as part of the X-ray image creation (Section 2.2), the QPB spectra were

constructed from a database of filter-wheel-closed data, scaled using data from the unexposed corner pixels (Kuntz & Snowden 2008). The QPB spectral subtraction was carried out prior to the spectral fitting described in the following section.

3. SPECTRAL ANALYSIS

3.1. Method

We carried out our spectral analysis using XSPEC[6] version 12.7.1d (Arnaud 1996), assuming Anders & Grevesse (1989) abundances. Our basic spectral model consisted of components representing (1) the foreground emission, (2) the Galactic halo emission, (3) the extragalactic background emission, (4) the HVC X-ray enhancement (for the on-enhancement spectra only), and (5) components of the instrumental background (instrumental fluorescence lines and soft proton contamination) that were not removed by the QPB subtraction. The details of these components are as follows.

1. We modeled the foreground emission using a single-temperature ($1T$) unabsorbed APEC model (Smith et al. 2001; Foster et al. 2012), the temperature of which was fixed at $kT = 0.1$ keV ($T = 1.2 \times 10^6$ K). Although the foreground emission in the *XMM-Newton* band is likely to be dominated by solar wind CX emission (e.g., Koutroumpa et al. 2007), such a foreground model can adequately model the foreground emission in CCD-resolution spectra (e.g., Galeazzi et al. 2007; Henley & Shelton 2008; Gupta et al. 2009). The emission measure of this component was a free parameter—we assumed that this emission measure was the same for the different spectral extraction regions (see below for a justification of this assumption).
2. We also used a $1T$ APEC model to model the diffuse Galactic halo emission. The temperature and emission measure of this component were free parameters. We assumed that these parameters were the same for the different spectral extraction regions (see below for a justification of the assumption that the halo is uniform).
3. We modeled the extragalactic background using the double broken power-law model described in Smith et al. (2007). The normalizations of the two components were rescaled so that the 0.5–2.0 keV surface brightness would match that expected from sources with fluxes below the source removal threshold of 2×10^{-15} erg cm^{-2} s^{-1} (2.99×10^{-12} erg cm^{-2} s^{-1} deg^{-2}, using data from Moretti et al. 2003 and Hickox & Markevitch 2006; see Section 3.1.3 of Henley & Shelton 2013).
4. We modeled the HVC X-ray enhancement with an additional $1T$ APEC model, whose temperature and emission measure were free parameters. This component was only present in the model for the on-enhancement spectra; in the model for the off-enhancement spectra, this component's normalization was fixed at zero.
5. We modeled the Al and Si instrumental fluorescence lines (at ≈1.49 and ≈1.74 keV, respectively) with Gaussians, whose parameters were independent for each exposure. (Note that the pn detector does not exhibit the Si fluorescence line.) We modeled the soft proton contamination using a power law not folded through the instrumental response (Snowden & Kuntz 2012). From each exposure, we extracted two spectra: an on-enhancement spectrum and an off-enhancement spectrum. For each such pair of spectra, the index of the soft-proton power-law model was the same, but the normalizations were independent. We originally tried tying together the normalizations according to the relative scaling given by the *XMM*-ESAS `proton_scale` program, but found that this led to poor fits above ∼2 keV. The soft proton model parameters were independent for each exposure.

The halo, enhancement, and extragalactic components were subjected to absorption, using the XSPEC `phabs` model (Bałucińska-Church & McCammon 1992; Yan et al. 1998). The column density was fixed at $N_{\rm H} = 1.6 \times 10^{20}$ cm^{-2}, calculated from the Schlegel et al. (1998) I_{100} maps, using the conversion relation from Snowden et al. (2000). Because we do not know exactly where the enhancement emission arises relative to HVC material, we typically ignored absorption by the HVC itself. In order to test the effect of ignoring absorption by the HVC, we also experimented with a variant of our model in which we increased the column densities attenuating the enhancement and extragalactic components in the on-enhancement spectra. Since the on-enhancement spectral extraction region lies mainly between the 3×10^{20} and 4×10^{20} cm^{-2} contours (see Figure 1), for this model variant we increased $N_{\rm H}$ by 3.5×10^{20} cm^{-2} for these two components.

We checked that the foreground and halo components of our model are indeed uniform by fitting the above-described model (excluding the enhancement component) to the off-enhancement spectra from the two observations, with the normalizations of the foreground and halo components independent for each observation (although we assumed the halo temperature was the same for both observations). The resulting normalizations from each observation were consistent with each other. In particular, the fact that the foreground normalizations were consistent implies that the level of solar wind CX emission is similar in the two observations.

Having confirmed the uniformity of the foreground and halo components, we fitted our full model to our complete set of 0.4–5.0 keV spectra simultaneously (a total of 12 spectra: an on-enhancement spectrum and an off-enhancement spectrum from each of *XMM-Newton*'s three cameras, from each of the two observations).

3.2. Results

The observed spectra and the best-fit model are shown in Figure 2, and the best-fit model parameters are shown in the first row of Table 2. The best-fit foreground emission measure is somewhat higher than the foreground emission measures we assumed in Henley & Shelton (2013). The best-fit halo temperature and emission measure are higher than the median values obtained by Henley & Shelton (2013), but are not outliers. Because our sky background model was determined from spectra extracted from the same observations as our on-enhancement spectra, the fact that the best-fit background parameters are higher than typical should not adversely affect our measurements of the on-enhancement spectrum.

The enhancement component is hotter than the halo component, and its emission measure is similar in magnitude to that of the halo component. The best-fit model parameters of the enhancement component imply an intrinsic 0.4–2.0 keV surface brightness of 2.6×10^{-12} erg cm^{-2} s^{-1} deg^{-2}. From the size of the on-enhancement spectral extraction region (25 arcmin^2) and the distance of the cloud (assumed to be 60 kpc), we obtain the intrinsic luminosity of the enhancement: 7.9×10^{33} erg s^{-1}.

[6] http://heasarc.gsfc.nasa.gov/xanadu/xspec/

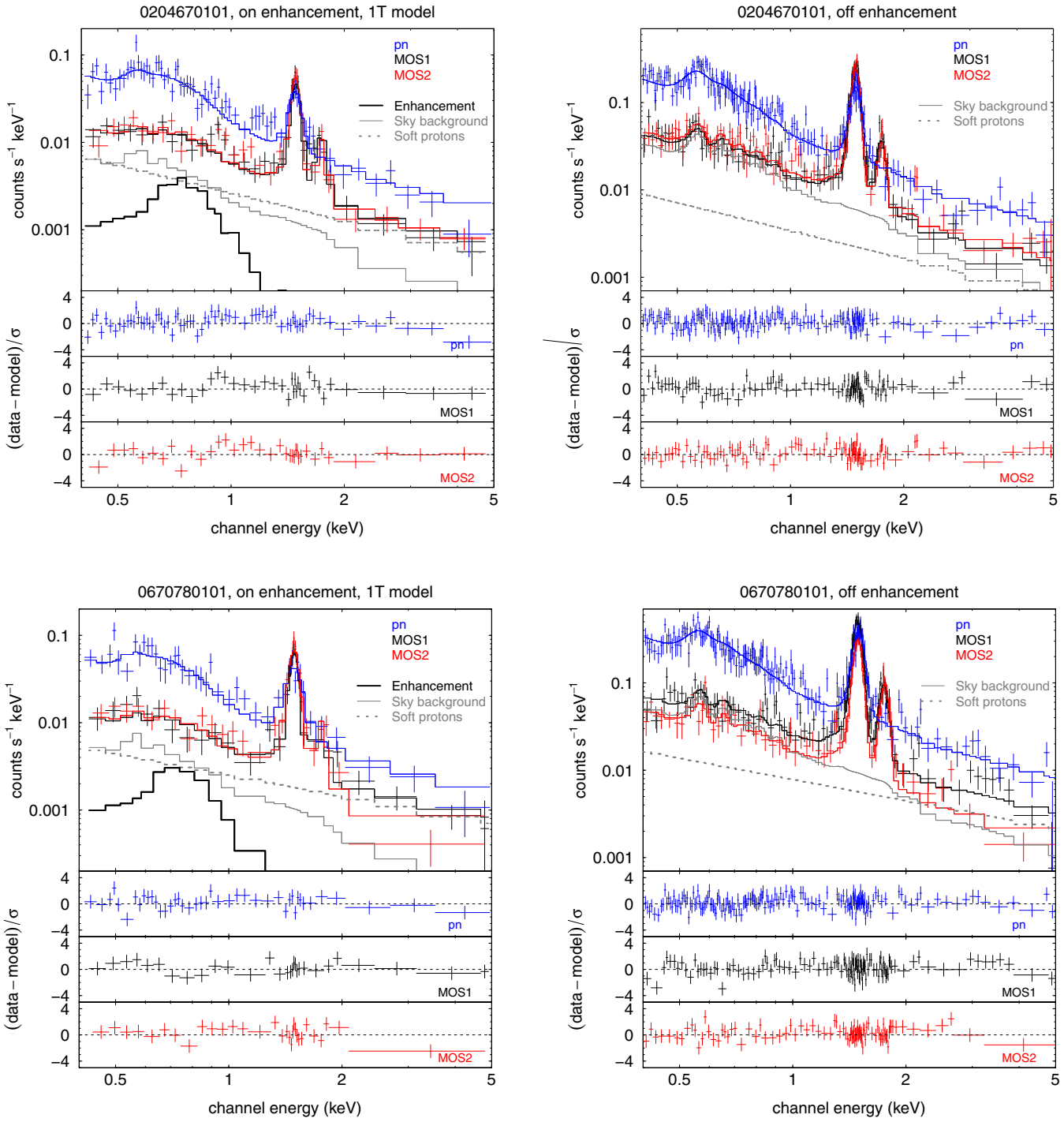

Figure 2. *XMM-Newton* spectra measured on (left) and off (right) the MS30.7 X-ray enhancement, from observations 0204670101 (top row) and 0670780101 (bottom row). In each plot, the main panel shows the X-ray spectra and best-fit models from each of the three *XMM-Newton* cameras (see legend for color code). For plotting purposes only, the spectra have been grouped such that each bin has a signal-to-noise ratio of at least three. Note that the count rates are higher for the off-enhancement spectra, as these were extracted from larger areas of the *XMM-Newton* cameras (see lower panel of Figure 1). In addition, we show the components of the best-fit MOS1 model—the enhancement itself, the sky background (foreground + halo + extragalactic), and the soft proton contamination are shown by a thick black line, a solid gray line, and a dashed gray line, respectively (to avoid clutter, we do not show the components representing the instrumental fluorescence lines). The three smaller panels under the main panel show the residuals for each camera.

(A color version of this figure is available in the online journal.)

While the fit shown in Figure 2 is reasonably good (reduced $\chi^2 = 1.07$), there are some features of the spectra that are not well fit. In particular, the on-enhancement spectra exhibit excess hard emission around 1 keV. This excess emission is more prominent in the obs. 0204670101 spectra; of the obs. 0670780101 spectra, the excess is most apparent in the MOS2 spectrum. Such excess emission is not apparent in the off-enhancement spectra, implying that the excess hard emission originates in the X-ray enhancement.

In Section 3.1, we described a variant of our basic spectral model in which we increased the column densities attenuating the enhancement and extragalactic components of the

Table 2
Spectral Fit Results

Model	Foreground[a]	Halo		Enhancement			χ^2/dof
	E.M. (10^{-3} cm^{-6} pc)	T (10^6 K)	E.M. (10^{-3} cm^{-6} pc)	T (10^6 K)	E.M. (10^{-3} cm^{-6} pc)	Ne/O (solar)	
Basic ($1T$)	$9.0^{+3.9}_{-0.9}$	$2.78^{+0.31}_{-0.09}$	$2.98^{+0.21}_{-0.25}$	$3.69^{+0.47}_{-0.44}$	$2.02^{+0.43}_{-0.28}$	1[b]	1824.52/1713
Non-solar Ne	$10.8^{+2.1}_{-0.8}$	$2.93^{+0.10}_{-0.09}$	$2.55^{+0.18}_{-0.21}$	$3.28^{+0.23}_{-0.35}$	$2.28^{+0.18}_{-0.40}$	$5.5^{+2.3}_{-1.4}$	1787.37/1712
$2T$	$11.3^{+1.4}_{-1.3}$	$2.95^{+0.13}_{-0.07}$	$2.52^{+0.16}_{-0.14}$	$2.60^{+0.36}_{-0.27}$	$1.99^{+0.58}_{-0.39}$	1[b]	1774.62/1711
				$11.9^{+1.1}_{-0.8}$	$1.58^{+0.30}_{-0.26}$	1[b]	
Recombining	$11.2^{+1.4}_{-1.0}$	$2.95^{+0.12}_{-0.08}$	$2.54^{+0.19}_{-0.21}$	$3.20^{+0.52}_{-0.63}$	See Table 3 for other parameters		1758.06/1706

Notes. Uncertainties are 90% confidence intervals for a single interesting parameter.
[a] The temperature of this component was fixed at 1.2×10^6 K (Section 3.1).
[b] Frozen.

on-enhancement spectra, to represent absorption by the HVC material itself. We found that this model resulted in an enhancement temperature 0.25×10^6 K lower than that in Table 2 (an insignificant difference, given the error bars), while the emission measure and luminosity were each 40% higher than those for the original model. None of these differences is large enough to affect the discussion of physical models of the X-ray enhancement in Section 4.

We experimented with some additional variants of our basic spectral model. These were attempts to improve the fit to the excess hard emission around 1 keV noted above. The results of these experiments are described in the following subsections.

3.2.1. Non-solar Neon Abundance

In this variant of the basic spectral model, we tried allowing the neon abundance of the enhancement component to be a free parameter. We concentrated on neon as its strongest lines are around 1 keV. The results are shown in the second row of Table 2. Most of the model parameters are not greatly affected. Thawing the neon abundance does improve the fit, but there is still some excess on-enhancement emission just above 1 keV (the enhanced neon abundance only really has an effect at ~0.9 keV, which is the location of Ne IX Kα). In addition, the best-fit neon abundance is rather high: ~6 times solar.

3.2.2. Two-temperature Plasma Model

We next tried a two-temperature ($2T$) plasma model for the X-ray enhancement (as opposed to the $1T$ model used above). The results for this model are shown in the third and fourth rows of Table 2 (the results for the hotter enhancement component are under those for the cooler component). The sky background components are not greatly affected. The cooler of the two enhancement components is somewhat cooler (2.6×10^6 versus 3.7×10^6 K) and fainter than the $1T$ enhancement model. This is because the hotter component can model the harder enhancement emission, leaving the cooler component free to shift to lower temperatures. Adding the second enhancement component improves the fit to the on-enhancement spectra around 1 keV—see Figure 3. However, the best-fit temperature of this component is very high (12×10^6 K). The best-fit model parameters for the $2T$ model imply 0.4–2.0 keV luminosities of 6.4×10^{33} and 7.1×10^{33} erg s^{-1} for the cooler and hotter components, respectively. The total luminosity of the $2T$ model is ~70% larger than that of the $1T$ model.

3.2.3. Recombining Plasma Model

In all the above spectral models, we assumed that the emission from MS30.7 is due to line emission from a plasma in collisional ionization equilibrium (CIE). In our final variant of our basic spectral model, we assumed that the emission is from an overionized, recombining plasma. We modeled the enhancement as a sum of radiative recombination continua. We used the XSPEC `redge` model, in which the flux is zero below the energy of the recombination edge, $E_{\rm edge}$, and varies with photon energy E as $\exp\left[-(E - E_{\rm edge})/kT\right]$ above the edge. Here, the temperature T is the electron temperature of the recombining plasma. We modeled the enhancement emission with five `redge` models, representing recombinations to H-like carbon, nitrogen, and oxygen and to He-like nitrogen and oxygen (the recombination edge for recombinations to He-like carbon is at 0.392 keV (Däppen 2000, Table 3.5), just below the *XMM-Newton* band that we are using). We detected three of the five edges, and for these edges we allowed the edge energies to vary from their expected values. For the other two edges, we fixed the edge energies at their expected values (from Däppen 2000, Table 3.5). We assumed that the electron temperature was the same for each recombination edge.

The results for this model are shown in the final row of Table 2 (sky background parameters and electron temperature of the recombining plasma), and in Table 3 (recombination edge energies and radiative recombination continuum fluxes). The electron temperature is similar to the temperature of the $1T$ CIE enhancement model. For the three detected edges, the measured edge energies are in good agreement with the expected values.

The best-fit models for the on-enhancement spectra are shown in Figure 4. This model fits the observed spectra well. In particular, as with the above-described $2T$ enhancement model, this recombining enhancement model leads to a much better fit to the on-enhancement emission around 1 keV than our basic $1T$ enhancement model. The intrinsic 0.4–2.0 keV luminosity of this model is 1.5×10^{34} erg s^{-1}, which is similar to that of the $2T$ enhancement model and approximately twice that of the $1T$ model.

For nitrogen and oxygen, we can use the ratios of the measured recombination fluxes to infer the N^{+6}/N^{+7} and O^{+7}/O^{+8} ion ratios, and hence the ionization temperatures of these two elements. If F_X is the flux due to recombinations from the $+X$ ion to the $+(X-1)$ ion, then $F_X \propto n_{\rm e} n_X R_X$, where $n_{\rm e}$ is the electron number density, n_X is the number density of the $+X$ ion, and R_X is the $+X \rightarrow +(X-1)$ radiative recombination

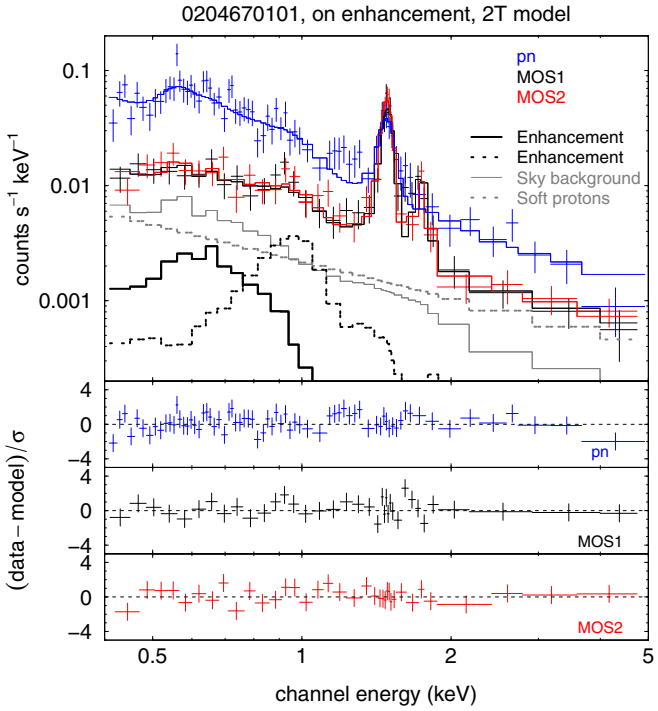

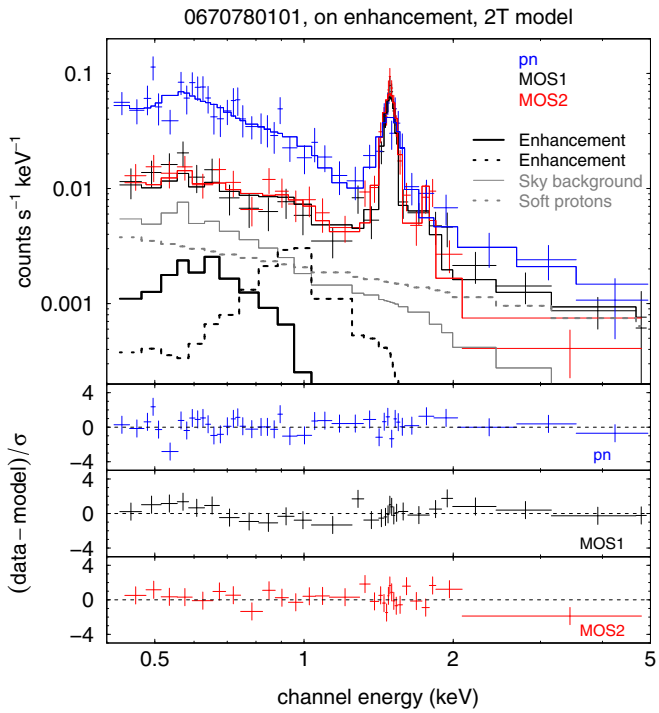

Figure 3. Same as the left panels of Figure 2, but using a 2T model to model the MS30.7 X-ray enhancement. The hotter enhancement component is shown by the dashed black line. The fits to the off-enhancement spectra (not shown) are similar to those in the right panels of Figure 2.

(A color version of this figure is available in the online journal.)

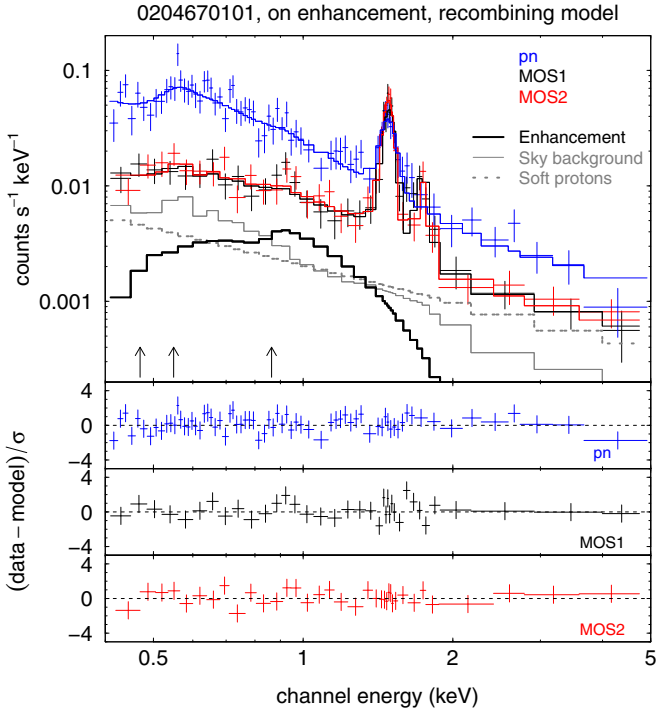

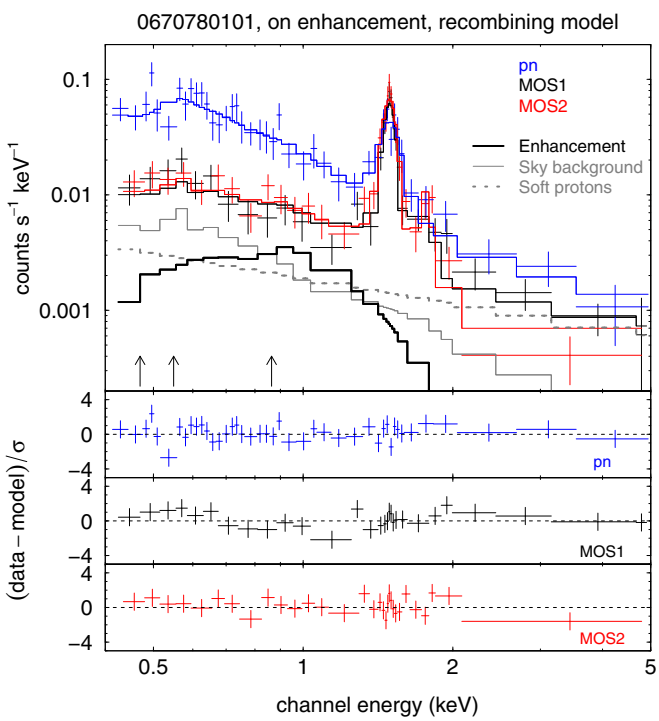

Figure 4. Same as the left panels of Figure 2, but using radiative recombination edges to model the MS30.7 X-ray enhancement (see text for details). For the enhancement model (thick black line), we have plotted the sum of the contributions from the individual recombination edges. The best-fit energies of the detected edges are indicated by the arrows (from left to right: $C^{+6}\rightarrow C^{+5}$, $N^{+6}\rightarrow N^{+5}$, and $O^{+8}\rightarrow O^{+7}$). The fits to the off-enhancement spectra (not shown) are similar to those in the right panels of Figure 2.

(A color version of this figure is available in the online journal.)

coefficient. Hence,

$$\frac{n_{X-1}}{n_X} = \frac{F_{X-1}}{F_X}\frac{R_X}{R_{X-1}}. \quad (1)$$

For oxygen, taking the upper limit of the $O^{+7} \rightarrow O^{+6}$ recombination flux and the lower limit of the $O^{+8} \rightarrow O^{+7}$ flux, we find $F_7/F_8 < 0.54$. The ratio of recombination coefficients is $R_8/R_7 = 1.69$ (Verner & Ferland 1996; we evaluated this ratio at $T = 3.2 \times 10^6$ K, the best-fit electron temperature for the recombining plasma, but in fact this ratio varies very slowly with temperature). Hence, $n_7/n_8 < 0.91$. This corresponds to

Table 3
Fit Results for Recombining Plasma Model

Recombination	Expected E_{edge}[a] (keV)	Measured E_{edge} (keV)	Flux (10^{-7} photons cm^{-2} s^{-1} arcmin^{-2})
$C^{+6} \rightarrow C^{+5}$	0.490	$0.470^{+0.043}_{-0.049}$	$5.1^{+7.5}_{-1.2}$
$N^{+6} \rightarrow N^{+5}$	0.552	$0.549^{+0.048}_{-0.072}$	$4.2^{+1.2}_{-1.1}$
$N^{+7} \rightarrow N^{+6}$	0.667	0.667[b]	<0.67
$O^{+7} \rightarrow O^{+6}$	0.739	0.739[b]	<0.48
$O^{+8} \rightarrow O^{+7}$	0.871	$0.864^{+0.044}_{-0.050}$	$1.60^{+0.51}_{-0.71}$

Notes. Uncertainties are 90% confidence intervals for a single interesting parameter. See the final row of Table 2 for the parameters of the sky background model and the electron temperature of the recombining plasma.
[a] Däppen (2000), Table 3.5.
[b] Frozen.

an ionization temperature for oxygen of $>2.8 \times 10^6$ K (using ionization balance data from Mazzotta et al. 1998).

Repeating the above analysis for nitrogen, we find $F_6/F_7 > 4.67$ (note that the "7" subscript now refers to N^{+7} rather than O^{+7}), $R_7/R_6 = 1.78$ (Verner & Ferland 1996; again, this ratio varies very slowly with temperature), and hence $n_6/n_7 > 8.3$, corresponding to an ionization temperature for nitrogen of $<1.3 \times 10^6$ K (Mazzotta et al. 1998). Note that the inferred ionization temperature for nitrogen is much lower than that for oxygen. Note also that the nitrogen ionization temperature is less than the electron temperature—in this situation, one would expect the nitrogen to be ionizing rather than recombining.

The fact that the nitrogen ionization temperature is less than the electron temperature suggests that our spectral model, which is characterized by a single electron temperature for the entire recombining plasma, may be overly simplistic. Unfortunately, our spectral data are insufficient to conclude whether or not recombination emission really is a major contributor to the observed emission—all we can do is note the improvement to the fit around 1 keV. However, because this model implies an oxygen ionization temperature that in turn implies a high shock speed (see Section 4.3), and because the luminosity of this model is similar (within a factor of two) to those of the $1T$ and $2T$ enhancement models, the conclusions of the following section, in which we discuss physical models of the X-ray enhancement, are the same whether we assume this model or a CIE model is the best description of the observed emission.

4. MODELS OF THE X-RAY ENHANCEMENT

In this section, we consider different physical models for the X-ray enhancement. In Section 4.2, we consider the possibilities that the emission is due to turbulent mixing of cold cloud material with a hot ambient medium, or to compression of such a medium by the cloud. We then examine the possibility that the observed emission is from a shock-heated plasma (Section 4.3). In Section 4.4, we consider CX reactions between the cold cloud and a hot ambient medium as a possible source of the emission. Finally, in Section 4.5, we return to the idea that the X-ray emission is from a hot plasma, but heated by magnetic reconnection rather than by a shock. However, before examining the individual models, we will first discuss the likely physical parameters for such models.

4.1. Model Parameters

The important physical parameters for the following models are the density, temperature, and magnetic field of the ambient medium, and the radius and speed of the cloud.

The ambient conditions in the vicinity of the Magellanic Stream are not well known. X-ray observations imply halo temperatures of $\sim$(1–3) $\times 10^6$ K (e.g., Kuntz & Snowden 2000; Yoshino et al. 2009; Henley & Shelton 2013; Gupta et al. 2014). It is uncertain out to what distance such temperature measurements are applicable. However, the conclusions reached below are not very sensitive to the ambient temperature.

For the density of a hot ambient medium, we will typically assume a value of 10^{-4} cm^{-3}. Bregman et al. (2009) point out that if the halo density were more than a few times 10^{-4} cm^{-3}, the dispersion measure would exceed the values measured toward some Large Magellanic Cloud (LMC) pulsars. For example, if the hot halo density were 5×10^{-4} cm^{-3} in the vicinity of MS30.7 (and presumably higher than this closer to the Milky Way), the dispersion measure toward the LMC ($d = 50$ kpc) would be $\geqslant$72 cm^{-3} pc: $\geqslant$25 cm^{-3} pc from the hot halo, plus 47 cm^{-3} pc from the warm ionized medium (using the best-fit model of Gaensler et al. 2008, and taking into account the LMC's Galactic latitude). In contrast, the two lowest dispersion measures measured toward the LMC are 45 and 65.8 cm^{-3} pc (there is some uncertainty as to whether the pulsar that yields the lower value is in the LMC or in the foreground; Manchester et al. 2006). Furthermore, if the hot halo density were 5×10^{-4} cm^{-3} out to a distance of at least 60 kpc (the assumed distance of MS30.7), the hot halo's emission measure would exceed 0.015 cm^{-6} pc. In contrast, analyses of the soft X-ray background emission typically yield halo emission measures of a few times 10^{-3} cm^{-6} pc (e.g., Kuntz & Snowden 2000; Yoshino et al. 2009; Henley & Shelton 2013; note that none of these studies report an emission measure exceeding 0.01 cm^{-6} pc).

In Section 4.3, we will consider the possibility that MS30.7 is ramming into material shed from a preceding cloud in the Stream. In this situation, the ambient material will have a higher density and a lower temperature than that discussed above. Note that, in this case, the higher ambient density will be relatively localized, and so will not violate the above density constraints.

When we discuss magnetic reconnection (Section 4.5), we will need to know the ambient magnetic field. There are no direct measurements of the ambient field strength in the vicinity of the Magellanic Stream. McClure-Griffiths et al. (2010) used extragalactic rotation measures to estimate the magnetic field in an HVC in the Leading Arm of the Magellanic System. They found that the line-of-sight component of the coherent magnetic field was $\gtrsim 6$ μG. However, it should be noted that this value pertains to the field within the cloud, which may be enhanced relative to the ambient field. Furthermore, this HVC is only

$\sim$10 kpc above the Galactic disk (using the distance assumed by McClure-Griffiths et al. 2010), compared with $\sim$60 kpc for MS30.7. If we assume equipartition between the ambient thermal and magnetic energy densities, the ambient magnetic field strength is

$$B_{\rm equip} = \sqrt{12\pi nkT} = (1.0\,\mu{\rm G})\left(\frac{n}{10^{-4}\ {\rm cm}^{-3}}\right)^{1/2}\left(\frac{T}{2\times10^6\,{\rm K}}\right)^{1/2}, \quad (2)$$

where n and T are the ambient density and temperature, respectively.

For the cloud itself, we will assume a radius $r \approx 50$ pc (from the size of the X-ray enhancement; Section 2.2). For the cloud speed, we will assume that the orbital speed of the Magellanic Stream is similar to those of the Magellanic Clouds. Kallivayalil et al. (2006a, 2006b) used the *Hubble Space Telescope* to measure the proper motions of the Magellanic Clouds. Combining these measurements with radial velocities measurements, they obtained speeds relative to the Galactic Center of 378 ± 18 and 302 ± 52 km s^{-1} for the LMC and the Small Magellanic Cloud (SMC), respectively. Here, we will follow Bland-Hawthorn et al. (2007), and assume an orbital speed of 350 km s^{-1} for the Magellanic Stream. Given the orbital speeds of the Magellanic Clouds, MS30.7's speed is unlikely to exceed $\sim$400 km s^{-1}.

4.2. Turbulent Mixing with or Compression of a Hot Ambient Medium

The X-ray enhancement could in principle arise from turbulent mixing of cool HVC material with a hot ambient medium, resulting in gas of intermediate density and temperature that is potentially brighter in X-rays than the background (Shelton et al. 2012). However, hydrodynamical simulations of HVCs traveling through hot (typically 1×10^6 K) ambient gas imply that, in practice, only slight enhancements in the X-ray emission result from turbulent mixing (Shelton et al. 2012, specifically, their Case A models). We re-examined the model spectra created by Shelton et al. from their A models, calculating the 0.4–2.0 keV surface brightnesses for comparison with the measured value for MS30.7. We ignored models A8–A10, as the clouds in these models were initialized with supersonic speeds, and so shock heating (discussed below) would tend to mask the effects of turbulent mixing. Of the remaining A models, we found that the brightest had a peak 0.4–2.0 keV surface brightness of 2.6×10^{-14} erg cm^{-2} s^{-1} deg^{-2} (model A1, at $t = 30$ Myr; at this time, the ambient density in the vicinity of the cloud is a few times 10^{-4} cm^{-3}). This is two orders of magnitude less than the intrinsic surface brightness of the MS30.7 X-ray enhancement (Section 3.2).

The X-ray enhancement could also result from the compression of a hot ambient medium by the cloud, where the increased density results in an increase in the X-ray brightness (Herbstmeier et al. 1995). Shelton et al. (2012) did not consider this mechanism in their study, but the faintness of their A models also rules this out as the mechanism responsible for the MS30.7 enhancement.

4.3. Shock Heating

4.3.1. Strong Shocks

If we assume that the X-ray-emitting plasma is due to shock heating, we can translate the measured temperature to a corresponding shock speed. First, let us consider a strong (i.e., high Mach number) shock. Such a strong shock could arise in the context of MS30.7 if the cloud were ramming into cool material shed from a preceding cloud. For material crossing a strong shock at speed v, the postshock temperature is (e.g., Dyson & Williams 1997)

$$T = \frac{3\bar{m}v^2}{16k} = (1.4\times10^5\,{\rm K})\left(\frac{v}{100\,{\rm km\ s^{-1}}}\right)^2, \quad (3)$$

where $\bar{m} \approx 1\times10^{-24}$ g is the average mass per particle. Note that the speed in the above expression is the speed at which material crosses the shock, which may be somewhat faster than the speed of the cloud, as the shock tends to move away from the cloud as the cloud and shock evolve, at least in the early stages of the cloud's evolution. Hydrodynamical simulations imply that the shock speed exceeds the cloud speed by $\lesssim$10% for strong shocks in cool and warm ambient media induced by initially round clouds (Shelton et al. 2012). Note also that, in practice, the average post-shock temperature behind an HVC's bow shock would be lower than that expected from Equation (3) for a number of reasons, especially if the cloud is traveling through relatively dense cool or warm gas: (1) gas toward the side of the cloud will hit the bow shock obliquely, reducing the postshock temperature, (2) the cloud will decelerate as it passes through the dense gas, weakening the shock, and (3) radiative cooling will be important in the dense shocked gas.

For the $1T$ enhancement model, the best-fit temperature of the enhancement (Table 2) implies a shock speed of 510 km s^{-1}. For the $2T$ enhancement model, the two components' best-fit temperatures correspond to shock speeds of 430 and 920 km s^{-1}, respectively. These speeds are unreasonably high for MS30.7, even allowing for the fact that the shock speed may be greater than the cloud speed (Section 4.1). A shock speed of 385 km s^{-1} (10% greater than the assumed orbital speed of the Magellanic Stream) would yield a postshock temperature that is about half the observed $1T$ value.

4.3.2. Shock Heating of a Hot Ambient Medium

If, instead of ramming into cool material, MS30.7 is traveling through a hot ($\sim10^6$ K) ambient medium, the Mach number will be lower than in the strong-shock case considered above. In this case, we can use the general formula relating the pre- and postshock temperatures, T_1 and T_2, respectively, to the preshock Mach number, M_1 (Shu 1992, Equation (15.37)):

$$\frac{T_2}{T_1} = \frac{[(\gamma+1)+2\gamma(M_1^2-1)][(\gamma+1)+(\gamma-1)(M_1^2-1)]}{(\gamma+1)^2M_1^2}. \quad (4)$$

For an ambient temperature of $T_1 = 1\times10^6$ K and for T_2 equal to the best-fit temperature of the $1T$ enhancement model (Table 2), the above equation implies $M_1 = 3.0$, or a shock speed of 460 km s^{-1} (the speed of sound in 1×10^6 K gas is $\approx$150 km s^{-1}). The best-fit temperatures of the $2T$ enhancement model imply shock speeds of 360 and 900 km s^{-1}, respectively.

As discussed in Section 4.3.1, the shock in front of an HVC may travel faster than the cloud itself. For a hot, low-density ambient medium, we find that the difference in speeds is greater than in a denser, cooler medium. We carried out one-dimensional simulations of shock tubes in which gas initially traveling at 400 km s^{-1} (representing HVC material) rams

into stationary low-density hot gas (hydrogen number density $n_H = 6.45 \times 10^{-5}$ cm^{-3}, $T = 10^6$ K) or denser warm gas ($n_H = 6.45 \times 10^{-3}$ cm^{-3}, $T = 10^4$ K). We found that the shocks propagated into the hot and warm stationary gas at $\approx$570 and $\approx$405 km s^{-1}, respectively. Hence, a cloud speed of $\sim$350 km s^{-1} (Section 4.1) could plausibly produce a post-shock temperature similar to that of our best-fit 1T enhancement model.

While a shock in a hot ambient medium could approximately reproduce the observed 1T temperature of the enhancement, the low density of the shocked material will result in emission much too faint to explain the observations. The shock speeds estimated above using Equation (4) imply shock compression ratios of $\sim$3 (Shu 1992, Equation (15.35)). If the ambient electron density in the vicinity of the Magellanic Stream is $n_e \sim 10^{-4}$ cm^{-3} (Section 4.1), then behind the shock $n_e^2 \sim 10^{-7}$ cm^{-6}. Since MS30.7 is traveling close to perpendicular to the line of sight,[7] the extent of the X-ray enhancement along the line of sight is likely similar to its extent on the sky (i.e., $\sim$100 pc; Section 2.2). This implies an emission measure of $\sim 10^{-5}$ cm^{-6} pc, two orders of magnitude less than the observed emission measures in Table 2.

The postshock emission measure could be increased by increasing the ambient density, but this density is unlikely to substantially exceed 10^{-4} cm^{-3} at the distance of the Magellanic Stream (Section 4.1). If we take 5×10^{-4} cm^{-3} as an upper limit on the ambient density in the vicinity of the Magellanic Stream, the postshock emission measure will be $\sim 2 \times 10^{-4}$ cm^{-6} pc, which is an order of magnitude smaller than the observed value. Our conclusion here, that shock heating of a hot ambient medium would result in emission that is too faint to explain the MS30.7 observations, is consistent with that in Section 4.2, where we stated that Shelton et al.'s (2012) Case A models implied that compression of a hot ambient medium would result in emission that is too faint (although in that case the compression was not necessarily via a shock).

4.3.3. Predictions from Shelton et al. (2012) HVC Models

We further investigated shock heating using the Case B hydrodynamical models of Shelton et al. (2012). In these models, the initially spherical cloud hits warm gas (possibly representing material shed from a preceding cloud; $T = 10^4$ K, $n_H = 6.45 \times 10^{-3}$ cm^{-3}), after passing through hot halo gas ($T = 10^6$ K, $n_H = 6.45 \times 10^{-5}$ cm^{-3}). Note that the temperatures and densities of the ambient gases match those of the stationary gases in the shock tube simulations described in Section 4.3.2. Shelton et al. ran models with and without radiative cooling enabled (Br and Ba, respectively). The model clouds had a range of initial speeds (200–400 and 200–600 km s^{-1} for the Br and Ba models, respectively). The number in each model's name (e.g., Ba3) indicates the model cloud's initial speed in units of 100 km s^{-1}. The Ba models were run for up to 28 Myr, with data output every 2 Myr. The Br models were run for 2 Myr, with data output every 40 kyr. (Br model data are also available at 2 Myr intervals beyond $t = 2$ Myr. However, we found that these models were too soft and faint to explain the observations, and we do not show the results for these later Br epochs below.)

For each epoch of each model, we calculated the spectrum averaged over a radius of 50 pc from the cloud center (for an observer looking directly along the cloud's velocity vector). The spectra were calculated assuming CIE (see Shelton et al. 2012 for more details of the spectral calculations). We did not subtract off the contribution from the ambient medium in the model, to avoid potentially having to deal with negative model count rates. However, the model ambient medium is over 1000 times fainter than observed X-ray enhancement, so if an HVC model well matches the observed brightness of the enhancement, the contribution from the model ambient medium will be negligible.

We compared the surface brightnesses of the above-calculated spectra with the intrinsic surface brightness of the X-ray enhancement inferred from the spectral fitting (Section 3.2). In addition, we used each model spectrum as the enhancement component of our spectral model (Section 3.1), with the normalization as a free parameter. From these fits, we obtained χ^2 as a function of model epoch for each model that we investigated, allowing us to see how well the predicted spectra match the shape of the observed enhancement spectrum.

The results are shown in Figure 5. Let us first look at the Br models. The fastest Br model cloud (Br4, $v = 400$ km s^{-1}) produces enough X-rays to match the measured surface brightness of the enhancement (upper panel of Figure 5(a)). This occurs at $t = 1$ Myr, after the cloud hits the warm gas at $t \sim 0.7$ Myr (it takes some time for the X-ray-emissive gas to build up). However, the resulting X-ray emission is too soft, and the fit to the observed spectra is poor (lower panel of Figure 5(a), and upper right plot of Figure 6). This is because the post-shock temperature expected for a 400 km s^{-1} cloud is $\sim$(2.2–2.7) $\times 10^6$ K (Equation (3), assuming that the shock travels up to 10% faster than the cloud), much lower than the measured temperature of 3.7×10^6 K (for the 1T model; Table 2). Higher cloud speeds would produce higher temperatures, but MS30.7 is unlikely to be exceeding $\sim$400 km s^{-1}. At earlier epochs, when the cloud is traveling through the hot ambient gas, the post-shock temperatures are higher ($>3.0 \times 10^6$ K from Equation (4)), the resulting emission is harder (upper left plot of Figure 6), and the fits to the observed spectra are better (lower panel of Figure 5(a)). However, because of the low density of the hot gas, the resulting emission is too faint to explain the observations (upper panel of Figure 5(a); see also discussion in Section 4.3.2). At later epochs, the X-ray emission fades away, due to radiative cooling of the hot gas, and the X-ray emission in the model is dominated by that from the hot background gas. The period of bright X-ray emission lasts less than 1 Myr.

The slower Br models produce qualitatively the same results as model Br4. However, in these slower models, the brightest emission is much fainter than the observed emission. Also, this bright emission fades away much more quickly (in model Br2, the X-ray brightening lasts for $\lesssim$0.1 Myr).

The Ba models with $v \geqslant 300$ km s^{-1} produce about enough, or more than enough X-rays to explain the MS30.7 emission for a few Myr after hitting the warm gas (upper panel of Figure 5(b)). However, only for cloud speeds $\gtrsim$500 km s^{-1} is the emission hard enough to produce reasonable fits to the observed spectra (lower panel of Figure 5(b), and lower row of Figure 6). This is consistent with the fact that the best-fit 1T enhancement temperature implies a shock speed of $\sim$500 km s^{-1} (Section 4.3.1). However, as noted earlier, such a speed is unreasonably high for MS30.7. Note also that even the hardest HVC model spectrum still underpredicts the on-enhancement emission around 1 keV.

The X-ray bright periods in the Ba models last longer than in the Br models, because radiative cooling is disabled (eventually,

[7] From the assumed orbital speed (350 km s^{-1}; Section 4.1) and the line-of-sight velocity (118 km s^{-1}; Bregman et al. 2009) of MS30.7, the angle between MS30.7's velocity vector and the line of sight is 70°.

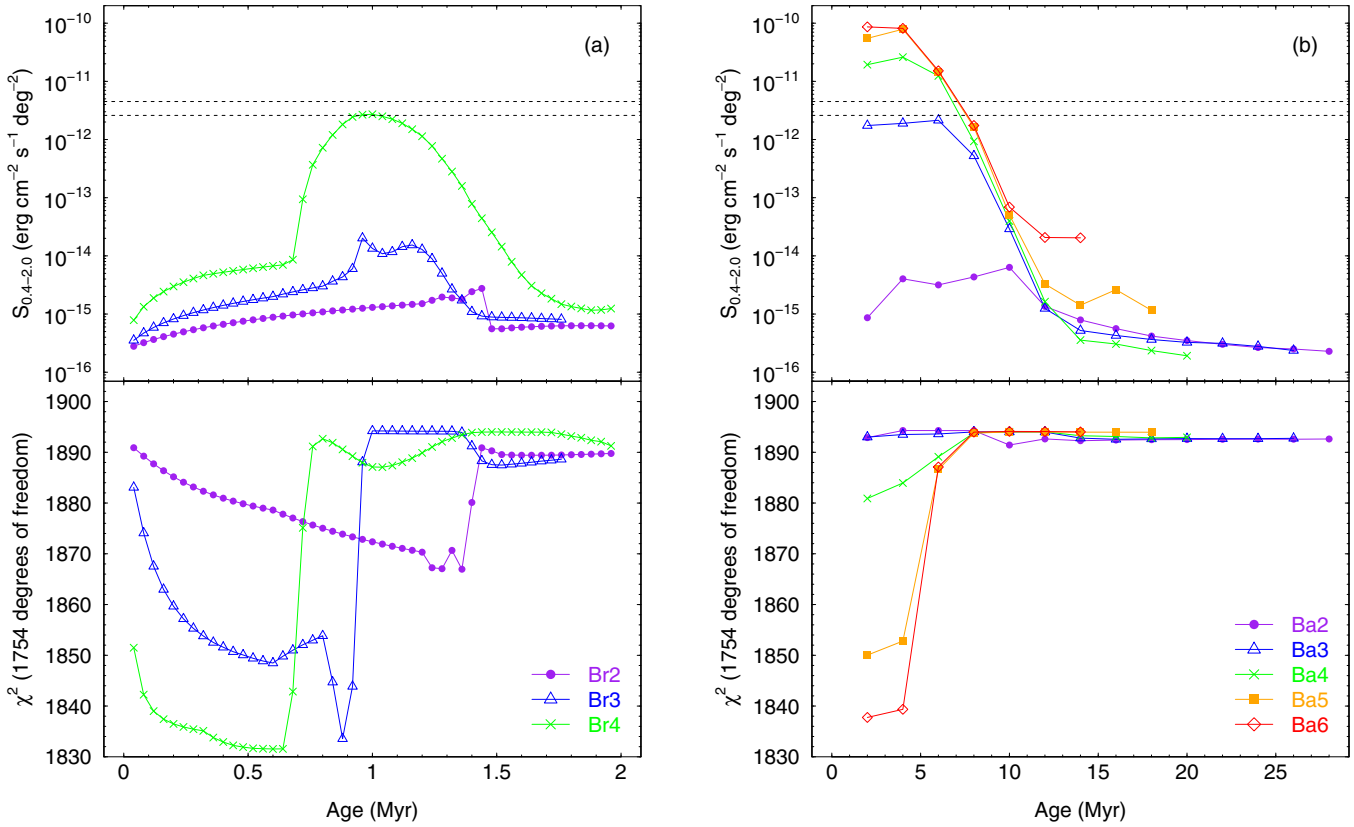

Figure 5. Intrinsic 0.4–2.0 keV surface brightnesses, $S_{0.4-2.0}$, of various HVC models from Shelton et al. (2012; top) and χ^2 from fits in which the MS30.7 X-ray enhancement is modeled using said HVC models (bottom), as functions of model epoch. Plot (a) shows the results for the Br models, in which radiative cooling was enabled, while plot (b) shows the results for the Ba models, in which radiative cooling was not enabled (note the different ranges on the time axes). The number in each model name indicates the model cloud's initial speed in units of 100 km s^{-1}. The horizontal dashed lines indicate the intrinsic surface brightnesses of the MS30.7 enhancement inferred from the 1T (lower line) and 2T (upper line) models (Section 3.2). Note that the number of degrees of freedom (1754) is larger than the numbers of degrees of freedom in Table 2, because here we fixed instrumental lines' energies and widths at the best-fit values obtained when fitting the 1T enhancement model (otherwise we found that XSPEC ran into problems during some of the fits).

(A color version of this figure is available in the online journal.)

adiabatic expansion and cooling causes the X-ray emission to fade away). In reality, subsolar abundances could suppress the radiative cooling rate, allowing the hot, X-ray-emissive gas to persist for longer than expected from the Br models. Lowering the abundances would also tend to lower the emissivity of the hot gas in the *XMM-Newton* band (note that the brightest Ba models overpredict the X-ray brightness at their earliest epochs; upper panel of Figure 5(b)).

4.3.4. Non-equilibrium Ionization

The model HVC spectra tested above were calculated assuming that the plasma in the hydrodynamical simulations was in CIE. Similarly, when we used Equations (3) and (4) to infer shock speeds from the temperatures of the 1T and 2T enhancement models, we were assuming that the observed X-ray enhancement is due to emission from a CIE plasma. In reality, the X-ray emitting plasma may be under- or overionized, relative to the plasma's electron temperature.

If the plasma is underionized, the resulting spectrum in the *XMM-Newton* band will be softer than that from a CIE plasma at the same electron temperature. Hence, for reasonable shock speeds, an underionized plasma would produce emission that is too soft to explain the spectrum of the enhancement.

In Section 3.2.3, we used a simple model of an overionized, recombining plasma to model the X-ray enhancement. This model yielded an electron temperature of 3.2×10^6 K, and an oxygen ionization temperature of $>2.8 \times 10^6$ K, corresponding to shock speeds of 480 and >450 km s^{-1}, respectively (Equation (3)).[8] Hence, as with the CIE enhancement models, MS30.7 appears to be traveling too slowly to explain the observed emission with a recombining plasma model. Furthermore, shock-heating typically results in gas that is underionized, rather than overionized. Overionization typically arises when gas undergoes rapid cooling (via radiation and/or adiabatic expansion), leaving the high ions frozen in. (These effects can be seen in Figure 4 of Shelton 1999, in the context of a supernova remnant: at earlier epochs, the shock-heated remnant is underionized, while at later epochs the cooling remnant is overionized.)

4.3.5. Summary of Shock Heating

Shock heating a hot ($\sim 10^6$ K), tenuous ($\sim 10^{-4}$ cm^{-3}) ambient medium results in emission that is too faint to explain the MS30.7 observations. In order to adequately model the MS30.7 X-ray enhancement, we require the cloud to be traveling at $\gtrsim$500 km s^{-1} through a cool or warm ($\lesssim 10^4$ K) medium of density $\sim 10^{-3}$ cm^{-3}. In contrast, MS30.7's speed is unlikely to exceed $\sim$400 km s^{-1} (Section 4.1). In the context of MS30.7, the denser warm ambient medium in the Shelton et al. (2012)

[8] We are considering only strong shocks in a cool or warm medium here, as shocks in a hot medium will likely lead to emission that is too faint.

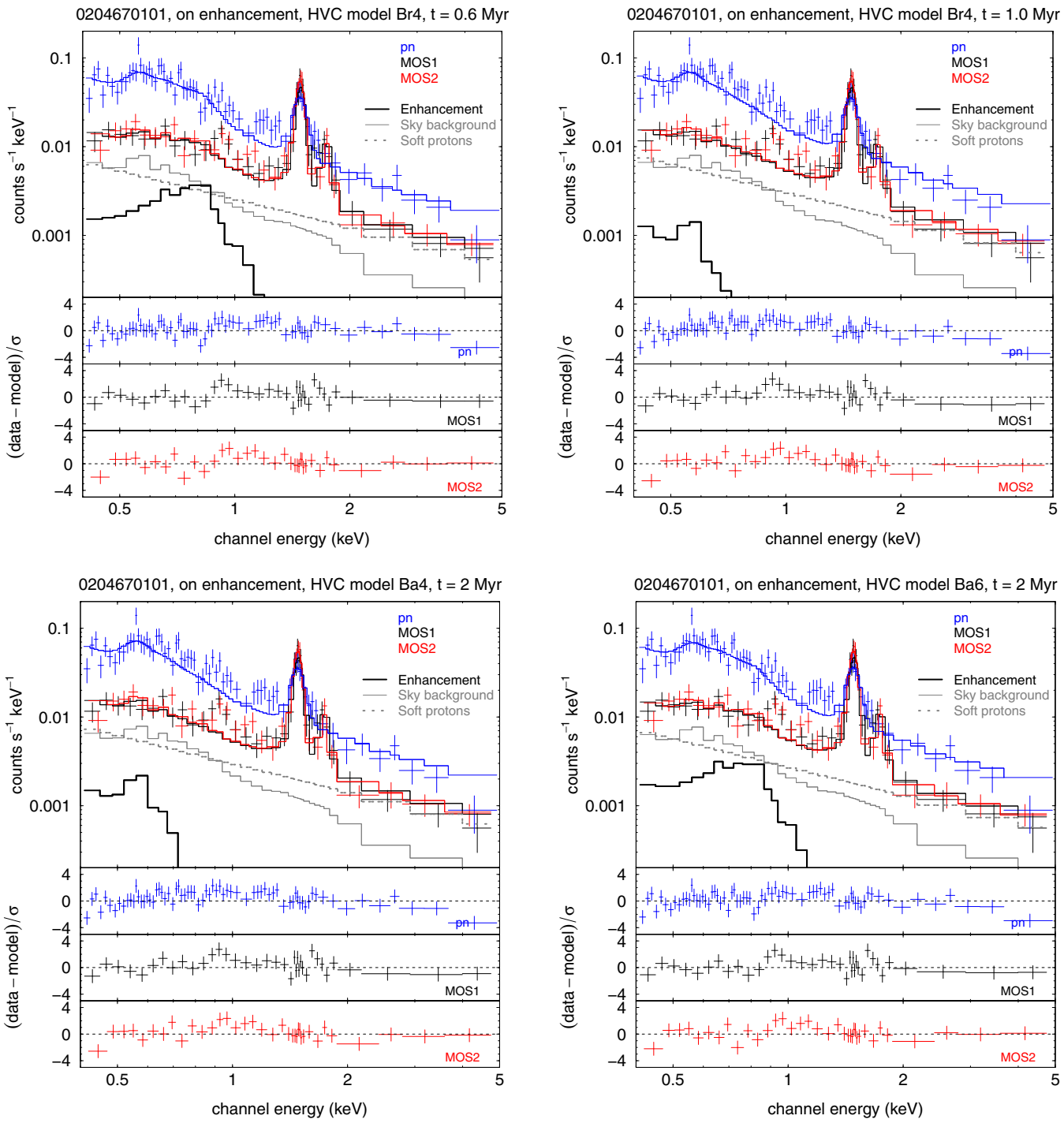

Figure 6. Same as the upper left panel of Figure 2, but with the HVC enhancement modeled using models from Shelton et al. (2012; see plot titles). The upper row shows the results for two different epochs of the Br4 model, before and after the cloud hits the warm gas. The upper right plot is from the epoch at which the Br4 model emission is brightest. The lower row shows the results for models Ba4 and Ba6, at $t = 2$ Myr.

(A color version of this figure is available in the online journal.)

models could represent material shed from a preceding cloud. In this case, the speed of MS30.7 relative to this material is likely to be even less than the orbital speed of the Magellanic Stream. We note that higher shock speeds could in principle be possible if a Galactic wind were impinging upon MS30.7. However, even if such a wind exists, at the distance of the Magellanic Stream it would likely be too tenuous to produce bright enough X-ray emission.

The above results therefore rule out simple shock heating as the origin of the MS30.7 X-ray enhancement. Note that Bregman et al. (2009) suggested that a shock driven into the cloud could be responsible for the X-ray emission. However, Shelton et al. (2012) found that such a reverse shock would not heat the cloud to X-ray-emitting temperatures—in their models, the emission comes from the shocked ambient medium.

4.4. Charge Exchange

Here we consider the possibility that CX between neutral atoms in the HVC and ions in an assumed hot ambient medium is

responsible for the observed X-ray emission. This CX emission will originate in a thin layer of thickness $l_{\rm CX}$, where $l_{\rm CX}$ is the mean free path of ions in the ambient medium undergoing CX with neutrals in the cloud (Lallement 2004). This mean free path is given by

$$l_{\rm CX} = \frac{1}{\sigma n_{\rm cl}} \approx \frac{d}{\sigma N_{\rm H}}, \quad (5)$$

where σ is the CX cross-section, $n_{\rm cl}$ is the cloud number density, d is the cloud diameter, and $N_{\rm H}$ is the column density of the cloud. The final part of the above expression assumes that the extent of the cloud on the sky is similar to that along the line of sight.

CX cross-sections are typically $\sim$ few $\times\ 10^{-15}\,{\rm cm}^2$ (e.g., Koutroumpa et al. 2006, Table 1), while the column density of the densest part of the cloud is $\sim 4 \times 10^{20}\ {\rm cm}^{-2}$ (see Figure 1). Hence, $l_{\rm CX}/d \sim$ (0.5–1) $\times\ 10^{-6}$; i.e., the CX emission is expected to arise in a very thin layer around the cloud. In fact, $l_{\rm CX}$ is an upper limit to the thickness of this layer, since some of the hydrogen in the cloud may undergo collisional ionization before it is able to undergo CX (Lallement 2004).

If the cloud is traveling at speed v through a hot ambient medium of density $n_{\rm h}$, the volumetric photon emissivity of a specific line, $\varepsilon_{\rm CX}$, due to CX is

$$\varepsilon_{\rm CX} = \sigma y n_{\rm cl} f A_X n_{\rm h} v, \quad (6)$$

where y is the yield of the line in question, f is the ion fraction for the ion responsible for the line (e.g., O^{+8} for an O VIII CX line), and A_X is the abundance of the relevant element. For a spherical cloud, the emission will arise in a thin hemispherical shell on the upwind side of the cloud, whose volume is $2\pi r^2 l_{\rm CX}$, where $r \approx 50$ pc is the cloud radius (Section 4.1). Hence, if the photon energy for the line in question is E, the total luminosity of the line is

$$L_{\rm line} = 2\pi r^2 E y f A_X n_{\rm h} v. \quad (7)$$

Note that this luminosity does not depend on the CX cross-section or the cloud density.

Equation (7) could be used to calculate a CX spectrum, provided the relevant line yields and ion fractions for the ambient medium were known. Here we take a different approach, and estimate the total luminosity due to CX. We introduce an efficiency, η_X, defined as the fraction of atoms of element X in the ambient medium that undergo CX reactions with the cloud's neutrals that lead to the production of X-ray photons within the energy band of interest (0.4–2.0 keV, in this case). For example, if oxygen in the ambient medium is mostly O^{+8} and O^{+7}, $\eta_{\rm oxygen}$ will be close to 1, as CX will typically result in O VII and O VIII lines in the band of interest. If oxygen is less highly ionized, $\eta_{\rm oxygen}$ will be smaller, as CX will typically not result in X-ray line emission.

Having defined η_X, let us define $\mathcal{E}$ as the typical energy of a CX line in the band of interest. Then, the total luminosity from a particular element due to CX is approximately $2\pi r^2 \mathcal{E} \eta_X A_X n_{\rm h} v$. If we sum over all astrophysically abundant elements that could contribute emission to the band of interest (C, N, O, Ne, Mg, Si, Fe), the total CX luminosity is

$$L_{\rm CX} \approx (8 \times 10^{32}\ {\rm erg\ s^{-1}}) \left(\frac{\mathcal{E}}{1\,{\rm keV}}\right) \left(\frac{\sum \eta_X A_X}{1.0 \times 10^{-3}}\right) \times \left(\frac{Z}{Z_\odot}\right) \left(\frac{n_{\rm h}}{10^{-4}\ {\rm cm^{-3}}}\right) \left(\frac{v}{350\,{\rm km\ s^{-1}}}\right), \quad (8)$$

where $Z/Z_\odot$ is the metallicity of the ambient medium relative to solar, and $v = 350\,{\rm km\ s^{-1}}$ is the assumed orbital speed of the Magellanic Stream (Section 4.1). Note that $\sum A_X = 1.0 \times 10^{-3}$ is the sum of the solar abundances of the aforementioned elements (Asplund et al. 2009), and so $8 \times 10^{32}\ {\rm erg\ s^{-1}}$ is an upper limit to the CX luminosity, calculated assuming solar abundances and that $\eta_X = 1$ for each element.

As noted in Section 3.2, the intrinsic 0.4–2.0 keV luminosity of the enhancement is $7.9 \times 10^{33}\ {\rm erg\ s^{-1}}$, 10 times larger than the luminosity given by Equation (8). (The luminosity of the enhancement is even higher if we use the $2T$ or recombining models; see Sections 3.2.2 and 3.2.3.) The only way CX could be bright enough to explain the observed emission is if the density of the ambient medium substantially exceeds $10^{-4}\ {\rm cm^{-3}}$, which is unlikely at such a large distance from the Milky Way (see Section 4.1).

4.5. Magnetic Reconnection

Finally, we consider magnetic reconnection as a possible source of the X-ray-emitting plasma. In general, magnetic reconnection occurs when magnetic field lines of different directions move toward each other. In such an encounter, the topology of the magnetic field can change, and energy stored in the magnetic field is released via particle acceleration, bulk motion of the plasma, and electric currents. These currents can then heat the plasma via Ohmic heating.

Zimmer et al. (1997) studied magnetic reconnection in the context of HVCs interacting with the magnetic field of the Galaxy. They first estimated the maximum temperature attainable by magnetic reconnection, by considering the equilibrium between the kinetic energy density of the cloud, the magnetic energy density, and the thermal energy density in the hot boundary layer in which the reconnection occurs. They estimated that temperatures of several million degrees should be attainable, much higher than the temperatures attainable with shock heating. They confirmed this estimate with magnetohydrodynamical (MHD) simulations. However, detailed spectral predictions which we could compare with our *XMM-Newton* observations are unavailable.

Although we wrote above of magnetic reconnection releasing energy stored in the magnetic field and heating the plasma, ultimately the energy seen in X-rays would come from the kinetic energy of the cloud. In the magnetic reconnection scenario, the cloud's motion through the Galactic magnetic field distorts the field, and the distorted field subsequently reconnects. We can place an upper limit on the rate at which the cloud's kinetic energy can be dissipated in this way by considering the rate at which the cloud does work against the ambient magnetic pressure, $P_{\rm mag} = B^2/8\pi$, where B is the ambient magnetic field strength. This rate is

$$L_{\rm mag} = \frac{1}{8} B^2 r^2 v = (1 \times 10^{35}\ {\rm erg\ s^{-1}}) \left(\frac{v}{350\,{\rm km\ s^{-1}}}\right) \left(\frac{B}{1\,\mu{\rm G}}\right)^2, \quad (9)$$

where we have again used $r = 50$ pc, $v = 350\,{\rm km\ s^{-1}}$ is the assumed orbital speed of the Magellanic Stream, and $B = 1\,\mu$G is the magnetic field strength estimated assuming equipartition (Section 4.1). We can also place a lower limit on the time, $t_{\rm mag}$, it would take for the cloud's kinetic energy, $E_{\rm K}$, to be completely dissipated via magnetic reconnection. If we assume that the cloud is spherical, the hydrogen number density is $n_{\rm H} = N_{\rm H}/2r$,

and the mass density is $\rho = N_{\rm H} m_{\rm H}/2rX$, where $m_{\rm H}$ is the mass of a hydrogen atom and $X \approx 0.7$ is the hydrogen mass fraction. Hence, $E_{\rm K} = \pi r^2 N_{\rm H} m_{\rm H} v^2/3X$, and

$$t_{\rm mag} \equiv \frac{E_{\rm K}}{L_{\rm mag}} = \frac{8\pi N_{\rm H} m_{\rm H} v}{3XB^2} = (9\ {\rm Gyr}) \left(\frac{v}{350\ {\rm km\ s^{-1}}}\right) \left(\frac{B}{1\ \mu{\rm G}}\right)^{-2}, \quad (10)$$

where we have used $N_{\rm H} = 4 \times 10^{20}$ cm^{-2} (see Figure 1).

The power given by Equation (9) is an order of magnitude larger than the 0.4–2.0 keV luminosity of the enhancement (Section 3.2). The time given by Equation (10), meanwhile, is several times the age of the Magellanic Stream (∼1.5–2 Gyr; e.g., Gardiner & Noguchi 1996; Nidever et al. 2008). It therefore seems that, from an energetics point of view, magnetic reconnection could plausibly power the observed X-ray emission from MS30.7.

5. DISCUSSION

5.1. Is the Emission Really from MS30.7?

Before we discuss our results, let us first consider again the possibility that the observed X-ray emission is not physically associated with MS30.7, but is the result of a chance alignment. We first considered this issue in Section 2.2—although we could not confidently rule out such a chance alignment, the morphology of the enhancement argues in favor of its being associated with MS30.7. Here, we specifically consider the possibility that the observed X-ray emission is due to a chance alignment with a background group of galaxies. Such objects exhibit X-ray temperatures of $\sim 10^7$ K (Osmond & Ponman 2004), similar to that of the hotter component of our $2T$ enhancement model (Section 3.2.2).

From the NASA Extragalactic Database (NED[9]), we find five galaxy groups within our mosaicked *XMM-Newton* field of view. One of these, MZ 01537, is centered at $(\alpha, \delta) = (00^{\rm h}13^{\rm m}38\overset{\rm s}{.}1, -27^\circ 10' 51'')$, on the eastern edge of the X-ray enhancement. This group is at a redshift of $z = 0.1264$. The size of this group is not stated, but assuming a typical group radius of ∼0.5 Mpc (Osmond & Ponman 2004), the radius on the sky is ∼3.′2 (from NED, calculated using the five-year *WMAP* cosmology parameters; Komatsu et al. 2009). The position and estimated size of MZ 01537 is shown by the dashed yellow circle in the lower panel of Figure 1.

The observed X-ray enhancement is located in the western half of the galaxy group, and beyond the group's estimated western edge. If the enhanced X-ray emission were from this galaxy group, we would expect the emission to be centered on the group's center. We therefore conclude that the X-ray enhancement is not associated with a background galaxy group.

5.2. Comparison with Bregman et al. (2009)

As stated in the Introduction, Bregman et al. (2009) reported an enhanced 0.4–1.0 keV pn count rate of 0.64 ± 0.10 counts ks^{-1} arcmin^{-2} toward the densest part of MS30.7. They obtained this value by extracting count rates from twenty equal regions around an annulus centered on the peak of the exposure map, with inner and outer radii of ≈4.′7 and ≈10.′5. Since this annulus was centered on the peak of the exposure map, the camera sensitivity was the same in all 20 regions, and so differences in the count rate correspond directly to differences in the observed X-ray surface brightness. Bregman et al. (2009) obtained an on-cloud count rate of 2.54 ± 0.09 counts ks^{-1} arcmin^{-2} from the three regions toward the densest part of the cloud, and a background count rate of 1.90 ± 0.05 counts ks^{-1} arcmin^{-2} from six regions to the southwest of the cloud. The difference between these two rates yields the count rate for the on-cloud enhancement quoted above.

From our best-fit $1T$ model of the enhancement, the 0.4–1.0 keV intrinsic surface brightness is 6.7×10^{-16} erg cm^{-2} s^{-1} arcmin^{-2}. We used PIMMS[10] to convert this to a count rate for the *XMM-Newton* pn camera with the thin filter, obtaining 0.64 counts ks^{-1} arcmin^{-2}.[11] Although this number is in exact agreement with Bregman et al.'s value, it should be noted that the PIMMS flux-to-count rate conversion is for an on-axis point source. As described above, Bregman et al. (2009) extracted their count rates from within an annular region centered on the peak of the exposure map. From the 0.4–1.0 keV pn exposure map, we find that the average sensitivity within this annular region is ∼60% of the peak sensitivity. Hence, the count rate inferred from our best-fit $1T$ model of the enhancement is ∼60% of the value quoted by Bregman et al. (2009). This discrepancy may indicate that our best-fit $1T$ model does not capture all of the soft X-ray emission from the enhancement, or that the soft-proton contamination was not uniform over the pn detector during Bregman et al.'s observation.

Bregman et al. (2009) state that their count rate measurement corresponds to a luminosity of 4×10^{33} erg s^{-1}, which is about half of the 0.4–1.0 keV luminosity derived from our best-fit $1T$ enhancement model, 7.2×10^{34} erg s^{-1} (note that this is only ∼10% less than the 0.4–2.0 keV luminosity reported in Section 3.2, as our best-fit $1T$ enhancement model produces little emission above 1 keV (see Figure 2)). It is unclear how this discrepancy in the luminosities arises, given that our best-fit model yields a count rate that is smaller than the value reported by Bregman et al. (2009).

5.3. The Origin of the X-Ray Emission

We examined models for the origin of the X-ray emission in Section 4. We found that neither turbulent mixing with or compression of a hot ambient medium (Section 4.2), shock heating (Section 4.3), nor CX (Section 4.4) can adequately explain the observed emission. Strong shocks in a cool or warm ambient medium result in emission that is too soft (for reasonable cloud speeds), while turbulent mixing, compression or shock heating of a hot ambient medium, and CX all result in emission that is too faint (for reasonable ambient densities).

Although we do not have spectral predictions that we can directly compare with our observations, magnetic reconnection appears to be the best explanation for the observed emission. Zimmer et al. (1997) found that this process could heat plasma to temperatures of several million degrees (much hotter than is possible with shock heating), and we argued that, from an energetics point of view, the resulting emission could be bright enough to match the observations (Section 4.5). However, if the magnetic field strength in the vicinity of the Magellanic

[9] http://ned.ipac.caltech.edu/

[10] http://cxc.harvard.edu/toolkit/pimms.jsp

[11] For this conversion we used $N_{\rm H} = 1.6 \times 10^{20}$ cm^{-2} (Section 3.1) and $\log T = 6.55$ (the nearest value to our measured temperature; Table 2).

Stream is substantially less than 1 μG, or if the efficiency with which the cloud's kinetic energy can be converted to thermal energy in the X-ray-emitting plasma is $\lesssim$0.1, then magnetic reconnection also has difficulty explaining the observed X-ray emission. Resistive MHD simulations are needed to determine the X-ray spectrum and brightness that would result from a MS30.7-like cloud interacting with the Galaxy's magnetic field. Such simulations would have to take into account the subsolar metallicity of the Magellanic Stream (Fox et al. 2013).

In Section 4, we concentrated on the spectrum and brightness of the observed emission. Let us conclude this discussion by considering the morphology of the emission. The Magellanic Stream in general (and MS30.7 in particular) is likely moving in the general direction of the Magellanic Clouds, which lie south to southeast of MS30.7. The X-ray emission is mainly to the north and west of the densest part of the cloud, i.e., on the downstream side of the cloud. In contrast, shock-heated gas is expected to be on the upstream side of the cloud (Shelton et al. 2012). Similarly, we pointed out in Section 4.4 that CX emission is expected to originate in a thin shell on the upstream side of the cloud.

Zimmer et al. (1997) suggested that magnetic reconnection would take place throughout the mixing layer between an HVC and the ambient medium, as the fluid flow in this mixing layer would tend to tangle up the field, bringing oppositely directed magnetic fields together at many different locations. In this scenario, we would expect to see X-ray emission all around the cloud, or possibly concentrated on the upstream side of the cloud, rather than concentrated on the downstream side. However, we suggest that it may be possible for magnetic reconnection to preferentially heat the plasma on the downstream side of the cloud. As an HVC moves through a magnetic field roughly perpendicular to its velocity vector, the field is drawn down into a "V" shape behind the cloud. This can be seen in two-dimensional MHD simulations of HVCs (Santillán et al. 1999, Figures 4–6; Jelínek & Hensler 2011, Figure 4), and is also reported to be seen in three-dimensional simulations (Kwak et al. 2009). If this V shape is sufficiently deep and steep-sided, the downward-pointing magnetic field on one side of the V will be adjacent to the upward-pointing field on the other side. Such a field configuration could allow magnetic reconnection to occur behind the cloud. Resistive MHD simulations would be needed to test whether or not this would occur in practice, i.e., do the oppositely directed magnetic fields in the V get close enough to each other for reconnection to take place?

6. SUMMARY AND CONCLUSIONS

We have presented our analysis of two *XMM-Newton* observations of the HVC MS30.7−81.4−118 (MS30.7), a constituent of the Magellanic Stream. We concentrated on the enhanced X-ray emission observed near the densest part of the cloud, initially reported by Bregman et al. (2009). This enhanced emission is concentrated to the north and west of the densest part of the cloud—this is likely the downstream side of the cloud. The X-ray enhancement is $\sim$6′ or $\sim$100 pc across (Section 2.2).

We first modeled the enhancement with a 1T thermal plasma model, obtaining a temperature of 3.7×10^6 K, and an intrinsic 0.4–2.0 keV luminosity of 7.9×10^{33} erg s^{-1} (Section 3.2). While the fit was reasonably good overall, the on-enhancement emission around 1 keV tended to be underpredicted. The fit could be improved by the addition of a second plasma component—in this 2T fit, the best-fit temperatures were 2.6×10^6 and 1.2×10^7 K, and the luminosity was $\sim$70% larger than that obtained with the 1T model (Section 3.2.2). The fit could also be improved by modeling the enhancement as a recombining plasma (Section 3.2.3). However, the fact that this model yields a nitrogen ionization temperature lower than the electron temperature ($<1.3 \times 10^6$ versus 3.2×10^6 K) suggests that, if recombination emission really is important, our recombining spectral model may be overly simplistic.

We examined several different physical models for the observed X-ray emission (Section 4; see also Section 5.3). Shock heating of hot, tenuous gas and of warm, denser gas results in emission that is too faint and too soft, respectively, while turbulent mixing, compression of a hot ambient medium, and CX all result in emission that is too faint. Magnetic reconnection appears to be the best explanation for the heating of the X-ray-emitting gas. Resistive MHD simulations are needed to test this conclusion. In particular, does magnetic reconnection dissipate the cloud's kinetic energy with sufficient efficiency to power the observed X-ray emission, and is the resulting emission concentrated on the downstream side of the cloud? If such simulations can explain the observed X-ray emission, then, as noted in the Introduction, the observed X-ray spectrum and brightness could potentially constrain the magnetic field in the vicinity of the Magellanic Stream.

We conclude by noting that there is no reason to think that MS30.7 is special. Other similar constituent clouds of the Magellanic Stream may exhibit X-ray emission. If magnetic reconnection is indeed responsible for the emission from MS30.7, and if the ambient conditions are reasonably uniform all along the Magellanic Stream, we might expect other clouds to be similar to MS30.7 in terms of the inferred plasma temperature, the X-ray luminosity, and the location of the X-ray-emitting plasma. This expectation could be tested with future observations.

We thank C. Brüns for providing us with the H I data shown in Figure 1. This research is based on observations obtained with *XMM-Newton*, an ESA science mission with instruments and contributions directly funded by ESA Member States and NASA. We acknowledge use of the R software package (R Development Core Team 2008). This research has made use of the NASA/IPAC Extragalactic Database (NED) which is operated by the Jet Propulsion Laboratory, California Institute of Technology, under contract with the National Aeronautics and Space Administration. This research was funded by NASA grant NNX12AI56G, awarded through the Astrophysics Data Analysis Program. K.K. was supported by the year 2013 Research Fund of the Ulsan National Institute of Science and Technology (UNIST).

REFERENCES

Anders, E., & Grevesse, N. 1989, GeCoA, 53, 197
Arnaud, K. A. 1996, in ASP Conf. Ser. 101, Astronomical Data Analysis Software and Systems V, ed. G. H. Jacoby & J. Barnes (San Francisco, CA: ASP), 17
Asplund, M., Grevesse, N., Sauval, A. J., & Scott, P. 2009, ARA&A, 47, 481
Bałucińska-Church, M., & McCammon, D. 1992, ApJ, 400, 699
Bland-Hawthorn, J., Sutherland, R., Agertz, O., & Moore, B. 2007, ApJL, 670, L109
Bregman, J. N. 2004, in High-Velocity Clouds, ed. H. van Woerden, B. P. Wakker, U. J. Schwarz, & K. S. de Boer (Astrophysics and Space Science Library, Vol. 312; Dordrecht: Kluwer), 341
Bregman, J. N., Otte, B., Irwin, J. A., et al. 2009, ApJ, 699, 1765
Brüns, C., Kerp, J., Staveley-Smith, L., et al. 2005, A&A, 432, 45
Cen, R., & Ostriker, J. P. 1999, ApJ, 514, 1
Collins, J. A., Shull, J. M., & Giroux, M. L. 2007, ApJ, 657, 271

Däppen, W. 2000, in Allen's Astrophysical Quantities, ed. A. N. Cox (4th ed.; New York: Springer), 27
Dyson, J. E., & Williams, D. A. 1997, The Physics of the Interstellar Medium (2nd ed.; Bristol: IOP)
Foster, A. R., Ji, L., Smith, R. K., & Brickhouse, N. S. 2012, ApJ, 756, 128
Fox, A. J., Richter, P., Wakker, B. P., et al. 2013, ApJ, 772, 110
Fox, A. J., Savage, B. D., & Wakker, B. P. 2006, ApJS, 165, 229
Fox, A. J., Savage, B. D., Wakker, B. P., et al. 2004, ApJ, 602, 738
Fox, A. J., Wakker, B. P., Savage, B. D., et al. 2005, ApJ, 630, 332
Gaensler, B. M., Madsen, G. J., Chatterjee, S., & Mao, S. A. 2008, PASA, 25, 184
Galeazzi, M., Gupta, A., Covey, K., & Ursino, E. 2007, ApJ, 658, 1081
Gardiner, L. T., & Noguchi, M. 1996, MNRAS, 278, 191
Gupta, A., Galeazzi, M., Koutroumpa, D., Smith, R., & Lallement, R. 2009, ApJ, 707, 644
Gupta, A., Mathur, S., Galeazzi, M., & Krongold, Y. 2014, ApJ, submitted (arXiv:1307.6195)
Henley, D. B., & Shelton, R. L. 2008, ApJ, 676, 335
Henley, D. B., & Shelton, R. L. 2013, ApJ, 773, 92
Herbstmeier, U., Mebold, U., Snowden, S. L., et al. 1995, A&A, 298, 606
Hickox, R. C., & Markevitch, M. 2006, ApJ, 645, 95
Hirth, W., Mebold, U., & Mueller, P. 1985, A&A, 153, 249
Jelínek, P., & Hensler, G. 2011, CoPhC, 182, 1784
Kallivayalil, N., van der Marel, R. P., Alcock, C., et al. 2006a, ApJ, 638, 772
Kallivayalil, N., van der Marel, R. P., & Alcock, C. 2006b, ApJ, 652, 1213
Kerp, J., Burton, W. B., Egger, R., et al. 1999, A&A, 342, 213
Kerp, J., Lesch, H., & Mack, K.-H. 1994, A&A, 286, L13
Kerp, J., Mack, K.-H., Egger, R., et al. 1996, A&A, 312, 67
Komatsu, E., Dunkley, J., Nolta, M. R., et al. 2009, ApJS, 180, 330
Koutroumpa, D., Acero, F., Lallement, R., Ballet, J., & Kharchenko, V. 2007, A&A, 475, 901
Koutroumpa, D., Lallement, R., Kharchenko, V., et al. 2006, A&A, 460, 289
Kuntz, K. D., & Snowden, S. L. 2000, ApJ, 543, 195
Kuntz, K. D., & Snowden, S. L. 2008, A&A, 478, 575
Kwak, K., Henley, D. B., & Shelton, R. L. 2011, ApJ, 739, 30
Kwak, K., Shelton, R. L., & Raley, E. A. 2009, ApJ, 699, 1775
Lallement, R. 2004, A&A, 422, 391
Lockman, F. J., Murphy, E. M., Petty-Powell, S., & Urick, V. J. 2002, ApJS, 140, 331
Manchester, R. N., Fan, G., Lyne, A. G., Kaspi, V. M., & Crawford, F. 2006, ApJ, 649, 235
Mathewson, D. S., Cleary, M. N., & Murray, J. D. 1974, ApJ, 190, 291
Mazzotta, P., Mazzitelli, G., Colafrancesco, S., & Vittorio, N. 1998, A&AS, 133, 403
McClure-Griffiths, N. M., Madsen, G. J., Gaensler, B. M., McConnell, D., & Schnitzeler, D. H. F. M. 2010, ApJ, 725, 275
Moretti, A., Campana, S., Lazzati, D., & Tagliaferri, G. 2003, ApJ, 588, 696
Muller, C. A., Oort, J. H., & Raimond, E. 1963, CRAS, 257, 1661
Nidever, D. L., Majewski, S. R., & Burton, W. B. 2008, ApJ, 679, 432
Osmond, J. P. F., & Ponman, T. J. 2004, MNRAS, 350, 1511
Putman, M. E., Staveley-Smith, L., Freeman, K. C., Gibson, B. K., & Barnes, D. G. 2003, ApJ, 586, 170
R Development Core Team. 2008, R: A Language and Environment for Statistical Computing (Vienna: R Foundation for Statistical Computing)
Santillán, A., Franco, J., Martos, M., & Kim, J. 1999, ApJ, 515, 657
Schlegel, D. J., Finkbeiner, D. P., & Davis, M. 1998, ApJ, 500, 525
Sembach, K. R., Wakker, B. P., Savage, B. D., et al. 2003, ApJS, 146, 165
Shelton, R. L. 1999, ApJ, 521, 217
Shelton, R. L., Kwak, K., & Henley, D. B. 2012, ApJ, 751, 120
Shu, F. H. 1992, The Physics of Astrophysics, Volume II: Gas Dynamics (Sausalito, CA: University Science Books)
Smith, R. K., Bautz, M. W., Edgar, R. J., et al. 2007, PASJ, 59, S141
Smith, R. K., Brickhouse, N. S., Liedahl, D. A., & Raymond, J. C. 2001, ApJL, 556, L91
Snowden, S. L., Freyberg, M. J., Kuntz, K. D., & Sanders, W. T. 2000, ApJS, 128, 171
Snowden, S. L., & Kuntz, K. D. 2012, Cookbook for Analysis Procedures for *XMM-Newton* EPIC MOS Observations of Extended Objects and the Diffuse Background, version 5.0, ftp://legacy.gsfc.nasa.gov/xmm/software/xmm-esas/xmm-esas.pdf
Verner, D. A., & Ferland, G. J. 1996, ApJS, 103, 467
Wakker, B. P., & van Woerden, H. 1997, ARA&A, 35, 217
Wakker, B. P., van Woerden, H., & Gibson, B. K. 1999, in ASP Conf. Ser. 166, Stromlo Workshop on High Velocity Clouds, ed. B. K. Gibson & M. E. Putman (San Francisco, CA: ASP), 311
Yan, M., Sadeghpour, H. R., & Dalgarno, A. 1998, ApJ, 496, 1044
Yoshino, T., Mitsuda, K., Yamasaki, N. Y., et al. 2009, PASJ, 61, 805
Zimmer, F., Lesch, H., & Birk, G. T. 1997, A&A, 320, 746